From Pore-Scale Reactive Transport to Reactor Performance: Quantifying Geomethanation Efficiency

Patrick Jasek[a,1,] *Gerald Stiedl*[a] *and Holger Ott*[a,*]

[a]Department of Geoenergy, Montanuniversität Leoben, Parkstraße 27, 8700, Leoben, Austria
[*]Corresponding author: holger.ott@unileoben.ac.at (H. Ott)

Abstract. Geomethanation in depleted gas reservoirs offers a route to couple subsurface hydrogen storage with in situ methane production, but its efficiency depends on the interaction between microbial growth, pore-space alteration, and gas–liquid mass transfer. Building on a coupled microfluidic–numerical workflow, we combine results from saturated and unsaturated experiments to quantify how pore-scale processes control reactor-scale performance. Under saturated conditions, biomass accumulation reduced porosity yet preserved substantial permeability because channel formation and intrinsic biomass conductivity maintained flow; simulations indicated an intrinsic biomass permeability of about 100 ± 50 mD, supporting continued advective nutrient supply. Under unsaturated conditions, gas injection shifted biomass from colony-dominated structures to a planktonic, interface-associated state, enhancing substrate access at gas–liquid boundaries. The integrated analysis showed methane evolution rates rising to about 0.30–0.35 mmol L^{-1} h^{-1}, while dimensionless evaluation identified predominantly reaction-limited behavior despite improved transport. Finally, this study establishes a workflow linking pore-scale morphology, transport regimes, and methane productivity for assessing geomethanation efficiency.

1 Introduction

The growing integration of intermittent renewable energy sources has intensified the need for large-scale storage concepts capable of balancing seasonal fluctuations in energy supply and demand. Among the available options, subsurface hydrogen storage in depleted gas reservoirs has gained increasing attention because such formations provide large storage capacities, established infrastructure, and proven gas tightness [1–4]. At the same time, these subsurface systems are not microbiologically inert. Indigenous microbial communities may consume injected hydrogen and trigger hydrogenotrophic conversion pathways, including methanation, thereby affecting storage efficiency, gas quality, and recovery performance [1–6].

Microbial growth in porous media has long been studied in relation to groundwater remediation, enhanced oil recovery, and bio-clogging, where biomass accumulation is known to reduce pore volume, redistribute flow, and alter permeability [7–10]. A key finding of this body of work is that biomass does not occupy pore space uniformly. Instead, microbial colonies and biofilms develop in spatially heterogeneous patterns, often preferentially in pore bodies, while preserving channels and voids that sustain advective transport [7–12]. These observations are highly relevant for geomethanation, where biomass-induced pore-space alteration may either hinder substrate delivery through clogging or enhance conversion by promoting longer residence times and localized reactive zones.

Microfluidic and lab-on-a-chip platforms provide a powerful means of studying such processes because they allow direct visualization of biomass accumulation within representative pore geometries under well-controlled hydraulic and chemical boundary conditions [11–14]. Previous lab-on-a-chip studies have demonstrated that pore-scale imaging can reveal coupled effects of microbial growth, transport limitation, and evolving flow paths that are difficult to resolve in conventional batch, column, or core-scale experiments [11–14]. In addition, these approaches enable time-resolved analysis of how biomass modifies hydraulic properties and how local transport conditions feed back on microbial organization. This makes microfluidics especially attractive for subsurface bio-reactive systems, where the interplay between microbiology and transport is inherently multiscale.

Despite this progress, important research gaps remain. First, many existing microfluidic studies focus on saturated systems and dissolved nutrient supply, whereas subsurface geomethanation in depleted gas reservoirs is commonly associated with unsaturated or two-phase conditions, in which gaseous H_2 and CO_2 coexist with brine and conversion depends strongly on gas–liquid mass transfer [5,6]. Second, prior work has mainly emphasized biomass accumulation and permeability impairment, while the connection between pore-scale biomass architecture and reactor-relevant performance indicators

* Corresponding author: holger.ott@unileoben.ac.at

such as methane productivity remains insufficiently constrained [7–14]. Third, only limited efforts have combined direct microfluidic observation with pore-scale numerical simulations in a way that permits a consistent interpretation of biomass growth, transport behavior, and effective process performance within one workflow [8,11,13–16].

The present work addresses these gaps by developing a coupled microfluidic–numerical workflow for reservoir-relevant geomethanation studies [15,16]. The workflow uses a high-resolution pore-network micromodel operated under anaerobic conditions with synthetic formation brine and methanogenic inocula, thereby enabling controlled observation of biomass accumulation under both saturated and unsaturated conditions [15,16]. Time-lapse microscopy is combined with digital image segmentation and direct numerical simulation to translate observed phase distributions into pore-scale models of flow and transport [15,16]. In this way, the experimental platform functions not only as a visualization tool, but as a lab-on-a-chip reactor concept with the capability to link microbial pore-space occupation, reactive transport, and reactor-relevant geomethanation efficiency.

The novelty of this research direction lies in its ability to bridge two traditionally separate perspectives: biofilm-induced pore-space alteration on the one hand, and reactor/process performance on the other. Rather than focusing exclusively on biomass growth or methane generation, the integrated workflow provides a framework for investigating how microbial organization, hydraulic accessibility, and interfacial substrate transfer jointly govern geomethanation in porous media. This offers a more mechanistic basis for evaluating depleted gas reservoirs as potential subsurface bioreactors for methane production from H_2 and CO_2.

2. Materials and Methods

2.1 Experimental concept and workflow

The applied methodology combines microfluidic experimentation with image-based numerical simulation to investigate geomethanation at the pore scale under reservoir-relevant conditions [5,6]. The workflow was designed to resolve biomass accumulation, pore-space alteration, hydraulic response, and reactive transport within the same experimental framework. It builds on an established microfluidic porous-media approach for microbial transport studies and extends it toward methanogenic hydrogen conversion in unsaturated systems [13]. The general procedure consisted of micromodel preparation, anaerobic inoculation, controlled substrate supply, time-resolved optical monitoring, pressure and gas analysis, and subsequent generation of segmented digital twins for direct numerical simulation [5,6].

2.2 Micromodel and microfluidic setup

Experiments were conducted in a borosilicate glass micromodel representing a two-dimensional porous network with a domain size of 20 mm × 10 mm and a uniform etching depth of 20 µm [5,6]. The model pore space was characterized by a porosity of 0.57, an initial permeability of 2.53 D, a total pore volume of 2.3 µL, and an average lateral pore size of approximately 170 µm [5,6]. The microfluidic setup comprised syringe-pump-controlled inlet and outlet flow, pressure monitoring, gas supply, and a high-resolution optical microscopy system for time-lapse imaging [5,6,13]. This configuration enabled controlled anaerobic operation and simultaneous visualization of biomass development and fluid displacement, see Figure 1.

2.3 Imaging and monitoring

Biomass accumulation and phase redistribution inside the pore network were monitored by high-resolution bright-field microscopy using an inverted microscope equipped with a digital camera and automated XY-stage scanning. This allowed stitched full-domain image acquisition with high spatial resolution and a time resolution of approximately 38 s per scan. In parallel, differential pressure signals were recorded throughout the experiments to quantify hydraulic changes caused by biomass growth and fluid redistribution. In the unsaturated workflow, methane production was additionally monitored by periodic gas sampling and micro-gas chromatography [5,6].

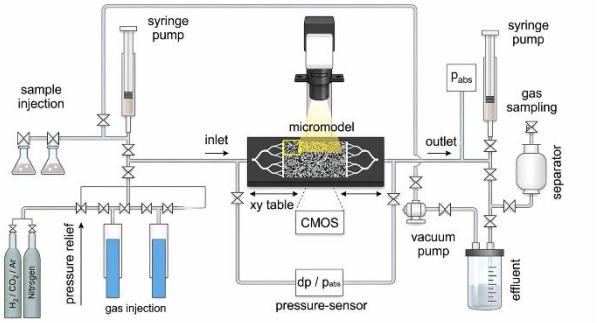

Figure 1. *Experimental setup for microfluidic geomethanation investigations. The system comprises sample and gas injection modules, syringe pumps, pressure control, a micromodel mounted on a microscope stage with illumination and CMOS imaging, as well as downstream gas sampling, phase separation, vacuum pumping, and effluent collection. The schematic illustrates the integrated flow routing and monitoring architecture used to control fluid delivery, observe pore-scale processes in real time, and quantify pressure and outlet conditions during the experiments*

2.4 Fluids and inocula

A chemically defined synthetic brine was prepared to reproduce the main hydrochemical characteristics of the formation water sampled from the test site in the Molasse Basin in Upper Austria, while ensuring reproducible experimental conditions [5,6]. The medium contained major salts, buffering components, reducing agents, vitamins, and trace elements and was prepared under strictly anaerobic conditions [5,6]. The brine composition was characterised using Inductively Coupled Plasma Optical Emission Spectroscopy (ICP-OES) for dissolved elemental concentrations, Ion Chromatography (IC) for major anions, and Liquid Chromatography with

Refractive Index Detection (LCRI) for dissolved organic compounds and fermentation products, see Table 1. Methanogenic inocula were derived from reservoir-relevant microbial systems and included both a defined hydrogenotrophic methanogen and mixed anaerobic consortia enriched from the same underground gas storage environment [5,6].

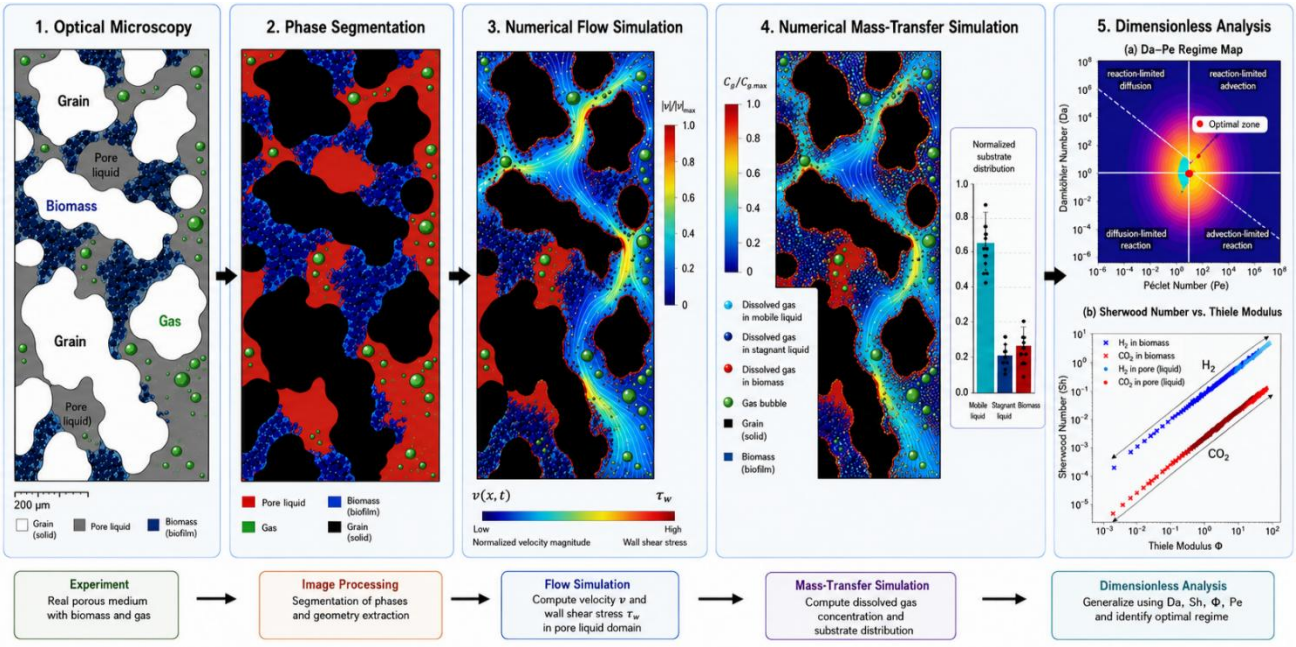

Figure 2. *Workflow for the analysis of bioreactive transport in a 2D micromodel. Time-resolved top-view microscopy images of the planar porous domain are used to identify representative phases, including gas, grain, and biomass, and to track their evolution over time. The experimental images are subsequently converted into segmented 2D phase maps, which serve as the basis for numerical flow and mass-transfer simulations on the same micromodel geometry. Regions of interest extracted from the simulated fields enable a localized assessment of transport behaviour, while the resulting metrics are further synthesized through dimensionless analysis to link pore-scale observations with governing transport regimes.*

Table 1. *Comparison of formation brine and synthetic brine (SB)*

Parameter	Formation brine	Synthetic brine (SB)
ICP-OES [mg/L]		
Al (Aluminium)	< 0.1	< 0.1
B (Boron)	17.8	27.7
Ca (Calcium)	410	284
Co (Cobalt)	< 0.02	0.06
Cr (Chromium)	< 0.16	< 0.16
Cu (Copper)	< 0.2	< 0.2
Fe (Iron)	95.8	< 0.36
K (Potassium)	1590	1850
Mg (Magnesium)	134	148
Mn (Manganese)	0.70	0.17
Mo (Molybdenum)	< 0.02	< 0.02
Na (Sodium)	9980	9570
Ni (Nickel)	0.07	0.09
P (Phosphorus)	< 2.0	8.4
Se (Selenium)	< 0.30	< 0.30
Zn (Zinc)	< 0.09	< 0.09
LCRI & IC [mg/L]		
Formic acid	62.6	81.6
Acetic acid	354.7	69.5
Ethanol	250.5	120.1
Isobutyric acid	16.9	–
Butyric acid	87.8	–
Isovaleric acid	12.7	–
Chloride	13209	11000
Nitrate	< LOD	–
Sulfate	< LOD	–
Hydrochemical parameters		
pH [–]	8.2	8.03
Conductivity [mS/cm]	29.5	29.1

2.5 Experimental procedure

Prior to each experiment, the flow system was evacuated to remove oxygen and verify leak tightness [5,6]. The micromodel was then saturated with growth medium and operated under controlled temperature and pressure conditions. In the saturated workflow, inoculated microbial suspension was injected into the fully brine-filled pore network and biomass accumulation was monitored during continuous flow [5]. In the unsaturated workflow, an initial colonization phase was followed by injection a stoichiometric H_2/CO_2-containing gas mixture (40 vol.% H_2 and 10 vol.% CO_2 in argon), establishing two-phase conditions with coexisting gas and brine [6]:

$$HCO_3^- + H^+ + 4H_2 \leftrightarrow CH_4 + 3H_2O \qquad (1)$$

$$\Delta G° = -131.0\ kJ\ mol^{-1}$$

This allowed the same platform to be used to study both biomass-induced hydraulic alteration and gas–liquid mass-transfer-controlled geomethanation at 40°C and 2,5 bar(g).

2.6 Image analysis and numerical simulation

Recorded image sequences were processed to segment the relevant phases within the porous domain [5,6]. Depending on the experimental condition, the segmented phases included grains, open pore space, biomass, and, in the unsaturated case, gas [5,6]. Image segmentation was performed using threshold-based and machine-learning-assisted approaches, after which the resulting geometries were converted into voxel-based digital twins for direct numerical simulation [5,6]. Flow calculations were carried out using a Stokes–Brinkman formulation to represent both free flow in the open pore space and Darcy-like flow through unresolved biomass regions [5,6]. In the unsaturated study, the simulations were further extended to evaluate local substrate transfer and transport characteristics within the evolving pore network [6].

2.7 Scope of the methodology

The combined method provides a direct link between experimental observation and numerical interpretation of pore-scale geomethanation processes, see Figure 2 [5,6]. Its main capability lies in resolving how microbial occupation of pore space modifies flow, transport accessibility, and reactive conditions in a reservoir-analog micromodel. By integrating an experimentally validated porous-media platform with digital analysis, the workflow establishes a basis for interpreting geomethanation not only as a microbiological process, but also as a transport-controlled reactor problem [5,6,13].

2.7.1. Methodology for Reactor Performance Calculation

A mechanistic reactor model was used to complement the dimensionless analysis and represent the main process sequence inside the micromodel. The calculation starts from the injected gas composition, the liquid-filled pore volume, and the microbial population. Microbial conversion becomes active only after H_2 and CO_2 dissolve into the aqueous phase. Accordingly, the model couples four steps: gas-phase definition, gas–liquid dissolution, microbial substrate conversion, and feedback on the evolving gas composition.

Solubility was calculated from Henry's law constants and corrected for temperature using the van't Hoff relation [17]. Effective gas–liquid transfer rates were included to estimate the dissolved substrate concentration available for methanogenesis. This is particularly relevant for H_2, whose low solubility commonly restricts biological Power-to-Gas methanation to a narrow reaction zone near the gas–liquid interface [24].

Microbial growth and methane formation were described using a double Moser-type kinetic model linked to H_2 and CO_2 availability, temperature sensitivity, and phase-specific transfer rates [23]. Substrate consumption was coupled stoichiometrically to CH_4 production, and simulated gas-phase concentrations were compared with experimental GC measurements to evaluate reactor performance.

Mass transfer across the interface was described using the classical two-film concept [25]. In this framework, gas and liquid bulk phases are assumed to be well mixed, whereas stagnant films at the interface control diffusive transport. Applied to the micromodel, this provides a simple mechanistic basis for connecting interfacial substrate transfer with observed methane evolution.

The starting point is the gas composition. Each gas species contributes to the total pressure according to its molar or volumetric fraction. The partial pressure of species i is calculated as:

$$p_i = y_i P \qquad (2)$$

where y_i is the gas-phase fraction of species i and P is the total pressure.

Since microorganisms consume dissolved substrates rather than the gas phase directly, the next step is to determine how much hydrogen and carbon dioxide can enter the aqueous phase. This is calculated with Henry's law:

$$C_i^* = k_{H,i}\, p_i \qquad (3)$$

where C_i^* is the equilibrium concentration of species i in the liquid phase and $k_{H,i}$ is the Henry coefficient.

However, equilibrium is not reached instantaneously. The transfer of gas into the liquid is governed by a concentration driving force. This is represented through a gas-water mass-transfer formulation:

$$r_i^{mt} = k_{gw,i}(C_i^* - C_i) \qquad (4)$$

where r_i^{mt} is the mass-transfer rate, $k_{gw,i}$ is the gas-water transfer coefficient, and C_i is the actual dissolved concentration in the liquid. This equation is essential because it defines how fast substrate becomes biologically available.

Once dissolved hydrogen and carbon dioxide are present, microbial activity is described through a substrate-limited growth expression. In simplified form, the specific growth rate is written as:

$$\mu = \mu_{phase}\left(\frac{H_2^2}{K_{H_2} + H_2^2}\right)\left(\frac{CO_2^2}{K_{CO_2} + CO_2^2}\right) f_T(T) \qquad (5)$$

where μ_{phase} represents the phase-dependent growth coefficient, K_{H_2} and K_{CO_2} are half-saturation constants, and $f_T(T)$ is the temperature correction factor.

The microbial population then evolves according to:

$$\frac{dX}{dt} = (\mu - k_d)X \qquad (6)$$

where X is the microbial abundance and k_d is the decay coefficient. This equation captures the balance between biomass growth and loss over time.

Methane formation is linked to biomass growth through stoichiometric yield relations. In simplified form, the

substrate consumption and product formation terms are given as:

$$r_{H_2} = -\left(\frac{1}{Y_{H_2}}\right)\frac{dX}{dt} \qquad (7)$$

$$r_{CO_2} = -\left(\frac{1}{4Y_{H_2}}\right)\frac{dX}{dt} \qquad (8)$$

$$r_{CH_4} = +\left(\frac{1}{4Y_{H_2}}\right)\frac{dX}{dt} \qquad (9)$$

where Y_{H_2} is the yield coefficient relating biomass growth to hydrogen consumption. These equations connect microbial growth directly to hydrogen depletion, carbon dioxide depletion, and methane production.

After each time step, the gas phase is updated to account for transfer into the liquid. In simplified form, the gas-phase balance is written as:

$$n_{g,i}(t + \Delta t) = n_{g,i}(t) - r_i^{mt} V_R \Delta t \qquad (10)$$

where $n_{g,i}$ is the amount of gas species i in the gas loop, V_R is the reactor volume, and Δt is the time step. This closes the coupling between gas phase and liquid phase and allows the reactor composition to evolve dynamically.

In the extended model, an additional retention or sink term can be introduced to represent delayed exchange with less accessible pore space or immobile regions. In a simplified first-order form, this can be written as:

$$r_{sink,i} = k_{sink,i} C_i \qquad (11)$$

2.7.2 Dimensionless analysis

To investigate reactive transport and kinetic behavior within the micromodel, a dimensionless analysis was performed. Temperature-corrected Henry's law constants, gas–liquid diffusivities, experimental methane production data, simulated velocity fields, and molar fluxes were combined to calculate characteristic transport and reaction numbers [17–19]. Effective diffusivities of H_2 and CO_2 in brine were estimated from established gas–liquid diffusion and porous-media transport correlations [18–20].

The Péclet number was used to distinguish advection- and diffusion-controlled regions, while first- and second-order Damköhler numbers were calculated to compare reaction and transport time scales [20]. In addition, the Sherwood number and Thiele modulus were evaluated to describe external and internal mass-transfer limitations, respectively [21,22]. The resulting parameters were mapped in Pe–Da space to identify transport-limited and reaction-limited domains across the micromodel. This framework links local pore-scale flow and substrate supply to reactor-scale geomethanation efficiency.

The first is the Peclet number, which compares advective transport with diffusive transport:

$$Pe = \frac{uL}{D} \qquad (12)$$

where u is characteristic velocity, L is characteristic length, and D is the diffusion coefficient. A low Pe indicates diffusion-dominated transport, whereas a high Pe indicates advection-dominated transport.

The second is the Damkohler number, which compares reaction rate k_r and transport timescales in its advective and diffusive form:

$$DaI = \frac{k_r L}{u} \ (13a), \quad DaII = \frac{k_r L^2}{D} \qquad (13b)$$

If $Da \ll 1$, the system is reaction-limited. If $Da \gg 1$, it is transport-limited.

To characterize gas-liquid transfer efficiency, the Sherwood number is used:

$$Sh = \frac{kL}{D} \qquad (14)$$

This number describes how efficiently interfacial transport is enhanced relative to diffusion alone.

When internal diffusion limitations within microbial clusters or biofilms are relevant, the Thiele modulus becomes useful:

$$\phi = L\sqrt{\frac{k}{D_{eff}}} \qquad (15)$$

A small ϕ indicates weak internal diffusion limitation, whereas a large ϕ suggests that only the outer parts of the reactive structure are effectively supplied.

2.7.3 Thiele modulus based on experimental reaction rates

To further quantify internal transport limitations within the reactive domain, the Thiele modulus is introduced. In contrast to classical formulations based on intrinsic rate constants, the present study derives the Thiele modulus directly from experimentally inferred reaction rates. This links pore-scale transport limitations to the observed reactor performance and avoids the need to prescribe an independent intrinsic kinetic constant.

The total reactive interfacial area is defined as:

$$A_{\mathrm{tot}} = a\,V \qquad (16)$$

where a is the specific interfacial area, and V is the reactor volume. Based on the experimentally derived molar conversion rate $\dot{n}$, an interfacial reaction flux can be formulated as:

$$r_s = \frac{\dot{n}}{A_{\mathrm{tot}}} \qquad (17)$$

where r_s represents the effective molar consumption rate per unit reactive surface area.
Using this definition, the Thiele modulus is expressed as:

$$\phi^2 = \frac{r_s\, a\, r_p^2}{D_{\mathrm{eff}}\, c_s} \qquad (18)$$

which can be rearranged to obtain a formulation directly dependent on measurable system parameters:

$$\phi^2 = \frac{\dot{n}\, r_p^2}{V\, f\, D_{\text{eff}}\, c_s} \qquad (19)$$

where r_p is the characteristic reactive length scale, D_{eff} is the effective diffusivity within the porous domain, c_s is the driving concentration at the interface, and f represents the fraction of the interface that is actively participating in the reaction.

This formulation allows the Thiele modulus to be evaluated without explicitly defining an intrinsic kinetic rate constant. The resulting value, therefore, provides a direct link between experimentally observed conversion rates and internal mass transport limitations.
A small ϕ indicates that diffusion within the reactive domain is sufficiently fast to supply substrate throughout the entire structure, resulting in a reaction-controlled regime. In contrast, a large ϕ signifies that diffusion is limiting, such that only regions close to the interface remain effectively supplied with substrate. In this case, the overall reactor performance becomes transport-limited despite potentially high intrinsic microbial activity.
In combination with the Damköhler and Sherwood numbers, the Thiele modulus provides a consistent framework to distinguish between kinetic limitation, interfacial transfer limitation, and internal diffusion limitation. This enables a mechanistic interpretation of reactor performance across scales.

5. Results and Discussion

5.1 Intrinsic biomass permeability and hydraulic alteration

The saturated micromodel experiments showed that biomass accumulation strongly altered the pore space but did not lead to complete hydraulic blockage. Instead, microbial growth produced heterogeneous biomass structures with preferential flow paths, preserving a finite permeability even at reduced porosity. This behavior confirms that biomass has to be treated as a conductive porous phase rather than as an impermeable solid obstruction.
By matching the experimentally measured pressure response with Stokes–Brinkman simulations on segmented digital twins, an intrinsic biomass permeability of **100 ± 50 mD** was determined [5]. The resulting permeability–porosity trend was described by a modified power-law relationship, consistent with earlier microfluidic porous-media work [13].

A critical observation was that permeability remained finite near the final biomass-occupied state because flow was maintained through a combination of open channels and permeable biomass domains [5]. This result is important for geomethanation because it indicates that microbial accumulation does not necessarily suppress substrate supply. As long as the intrinsic biomass permeability remains above a critical threshold, advective nutrient transport can persist through or around biomass clusters. In the saturated case, the calculated transport behavior therefore supports a scenario in which biomass growth modifies the pore network but still maintains hydraulic connectivity. This provides the basis for the unsaturated workflow, where gas–liquid interfaces and brine mobility additionally control substrate delivery [6].

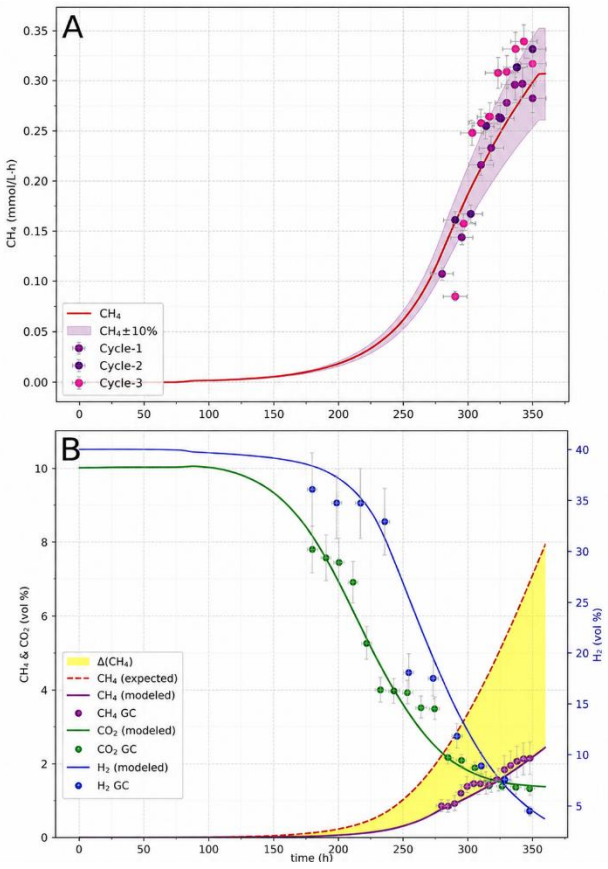

Figure 3. *(A) Modeled CH_4 production shown in red with a ±10% uncertainty band, compared with microGC-derived CH_4 concentrations from cycles 1-3. (B) Modeled gas-phase composition showing H_2 depletion on the right axis, CO_2 consumption, and CH_4 accumulation, together with microGC measurements and associated error bars. The agreement between modeled trends and experimental data captures the hydrogenotrophic conversion yield. The progressive increase in CH_4 yield across cycles suggests enhanced biomass exposure to the substrate gases and improved interfacial gas-liquid exchange.*

5.2 Reactor performance under unsaturated conditions

Under two-phase operation, the micromodel acted as a reactive lab-on-a-chip reactor in which H_2 and CO_2 were supplied through the gas phase and converted after dissolution into the aqueous phase. Methane production increased over successive gas-cycling phases, indicating improved microbial exposure to the substrate gas and enhanced gas–liquid exchange. After an initial low-production period, the methane evolution rate reached approximately **0.30–0.35 mmol L^{-1} h^{-1}** after extended cycling, and the mechanistic reactor model reproduced the measured microGC data well [6].

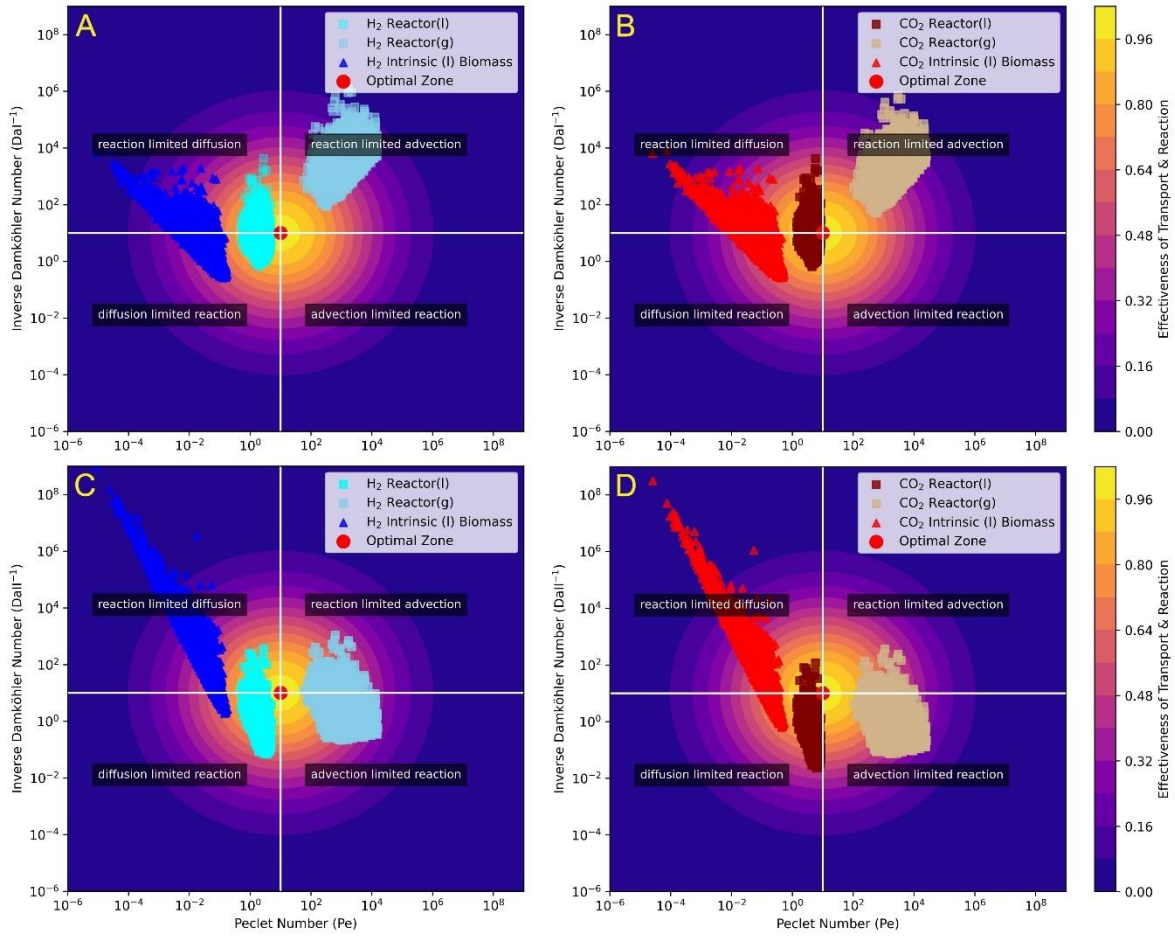

Figure 4. *Bioreactive transport maps for H_2 (left) and CO_2 (right), plotted on log–log scales as Péclet number on the x-axis versus inverse Damköhler number, on the y-axis for the advection–reaction representation (A, B). The background heatmap qualitatively indicates increasing overall transport–reaction effectiveness toward the warm central region. White reference lines mark the balanced transport–reaction condition at Pe=10 and Da^{-1}=10. In the diffusion–reaction representation shown in the lower panels (C, D), the y-axis denotes the inverse type-II Damköhler number.*

The reactor model coupled gas-phase composition, Henry's-law-controlled gas dissolution, gas-liquid mass transfer, microbial growth kinetics, and stoichiometric methane formation. Figure 3 compares three different methane responses: (i) the *expected* methane concentration, corresponding to the theoretical maximum methane yield calculated from the stoichiometric conversion of the injected hydrogen and carbon dioxide according to Eq.1, assuming complete substrate utilization and no transport or kinetic limitations; (ii) the *modelled* methane concentration, obtained from the coupled reactive transport model including gas dissolution, interfacial mass transfer, microbial growth, and biomass-related transport limitations; and (iii) the *measured* methane concentration determined experimentally. The agreement between the modelled and measured gas compositions indicates that the observed methane evolution can be explained by the coupled effects of gas-liquid mass transfer and microbial conversion rather than by stoichiometric substrate availability alone. The deviation between the theoretical (expected) and modelled responses demonstrates that interfacial transfer limitations, biomass accessibility, and the spatial distribution of the aqueous phase constrain the achievable methane yield. These findings highlight the central role of gas-liquid contact area, brine distribution, and biofilm accessibility in determining reactor performance and conversion efficiency [6].

5.3 Dimensionless interpretation of transport limitations

The dimensionless analysis was used to distinguish transport limitations acting at different spatial scales within the geomethanation system. For this reason, two Damköhler numbers were considered.

The first Damköhler number, DaI, compares the intrinsic microbial reaction rate with advective transport across the reactor or pore-network scale. It therefore describes whether substrates are supplied fast enough by flow to sustain microbial conversion. Low DaI indicates that advective transport is faster than microbial consumption, whereas high DaI indicates that the overall reactor behavior becomes limited by substrate delivery.

The second Damköhler number, DaII, compares microbial reaction with local diffusive transport. This number is related to diffusion through aqueous films, stagnant liquid regions, and biomass or biofilm domains. In this sense, DaI represents global transport limitation by

advection, while DaII represents local transport limitation by diffusion.
The Péclet number was used to distinguish whether transport is dominated by advection or diffusion. Reactor-scale Péclet numbers describe transport through the connected pore network, whereas biomass-scale Péclet numbers describe transport within or around biomass clusters. Gas-phase transport was treated separately because H_2 and CO_2 can be supplied efficiently through the gas phase, but microbial conversion occurs only after transfer into the aqueous phase and access to biomass.

In the saturated experiments, the liquid phase occupied the pore network continuously. Therefore, reactor-scale liquid transport describes substrate delivery through brine-filled pathways. Under these conditions, biomass permeability remained sufficiently high to allow advective nutrient supply, which explains why microbial activity could be sustained despite biomass accumulation.

In the unsaturated experiments, the gas phase provided efficient advective transport of H_2 and CO_2. However, this did not directly translate into higher methane production, because the substrates first had to dissolve into the aqueous phase, cross the gas-liquid interface, and diffuse toward biomass. Therefore, the limiting step shifted from bulk gas supply to gas-liquid mass transfer and local diffusion through the aqueous and biomass domains.

The term "reactor (l)" refers to the liquid-phase transport regime at the reactor or pore-network scale. In saturated systems, this corresponds to transport through the connected brine-filled pore space. The term "reactor (g)" refers to gas-phase transport in unsaturated systems, where connected gas pathways allow rapid advective supply. The term "intrinsic biomass (l)" refers to transport local to the biomass phase in the aqueous environment. It is relevant to both saturated and unsaturated systems because microbial conversion occurs in hydrated biomass or biofilm regions, not directly in the gas phase.

The transport-reaction effectiveness was calculated by comparing the transport-limited microbial conversion rate with the theoretical rate expected from intrinsic microbial kinetics and stoichiometric substrate availability. Effectiveness values close to 1, or 100%, indicate that transport is sufficiently fast and the microbial reaction can proceed near its intrinsic rate. Lower effectiveness values indicate increasing transport limitation, either by insufficient advective supply, slow gas–liquid transfer, or diffusion limitation inside the aqueous or biomass domains.
The optimal zone was defined as the region where substrate supply and microbial conversion are balanced. In this zone, Péclet numbers are high enough to maintain substrate renewal by advection, while Damköhler numbers remain moderate enough to avoid strong concentration gradients and local substrate depletion. Outside this zone, the system becomes inefficient either because transport is too weak to sustain reaction, or because reactants pass through the system without sufficient residence time for microbial conversion [6].

Overall, the Pe-Da framework shows that reactor performance is controlled by the coupling between global advective transport, local diffusive accessibility, gas–liquid mass transfer, and microbial conversion. The unsaturated experiments are controlled by gas-phase delivery followed by dissolution, interfacial transfer, and diffusion through the aqueous biomass environment. This explains why methane production cannot be predicted from stoichiometric substrate availability alone.

The Sherwood-Thiele analysis further showed that H_2 and CO_2 experience different mass-transfer constraints. H_2 occupied a higher Sherwood range, while CO_2 showed lower Sherwood numbers and stronger sensitivity to boundary-layer control because of its different solubility and diffusivity [6]. The effectiveness-factor interpretation indicated that, for the investigated operating window, internal diffusion limitations inside biomass were relatively weak when the Thiele modulus was low. Overall performance was therefore controlled mainly by external mass transfer, interfacial renewal, and the distribution of mobile brine rather than by diffusion inside the biomass alone, see Figure 5 [6].

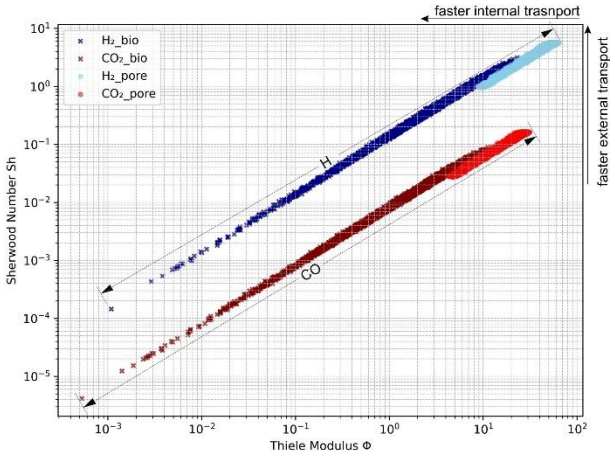

Figure 5. *Sherwood number (Sh) plotted against Thiele modulus (Φ) for H_2 and CO_2 at the biofilm and pore scales. The x-axis represents the severity of internal diffusion–reaction limitation, whereas the y-axis reflects gas–liquid mass transfer and diffusive delivery toward the biomass. H_2 occupies a high-Sh regime across $\Phi \sim 10^{-3}$ -10^{2} with $Sh_{bio} \sim 10^{-4}$ -10^{1} and $Sh_{pore} \sim 10^{0}$ -10^{1} indicating efficient external transfer and limited internal concentration gradients. In contrast, CO_2 exhibits Sh values one to two orders of magnitude lower at comparable Φ, suggesting stronger boundary-layer control and greater sensitivity to interfacial gradient renewal. The separation between biofilm- and pore-scale trends reflects the transport penalty imposed by tortuous porous pathways and reduced effective diffusivity relative to the intrinsic biofilm scale.*

5.4 Implications for geomethanation efficiency

The study shows that geomethanation efficiency is governed by two linked mechanisms. First, biomass must remain hydraulically accessible; the measured intrinsic biomass permeability of 100 ± 50 mD indicates that methanogenic biomass can maintain conductive pathways under saturated conditions [5]. Second, under gas-rich conditions, substrate availability is controlled by gas–liquid

transfer and the spatial contact between gas, brine, and biomass [6].

The optimal operating window identified by the dimensionless analysis lies near the transition where advection improves substrate delivery without excessive flushing or depletion. In practical terms, increasing flow alone is unlikely to improve conversion if gas-liquid transfer and biomass accessibility remain limiting. More effective improvements should target interfacial renewal, brine connectivity, biomass distribution, and maintenance of reactive surface area. Thus, the combined workflow links pore-scale biomass permeability to reactor-scale methane productivity and provides a quantitative basis for evaluating depleted gas reservoirs as subsurface bioreactors for geomethanation.

6. Discussion and Way Forward

The combined workflow shows that geomethanation in porous media cannot be evaluated from microbial activity or transport properties alone. Instead, reactor performance emerges from the interaction between biomass architecture, hydraulic connectivity, gas–liquid mass transfer, and local substrate availability. The saturated experiments demonstrate that microbial accumulation modifies the pore space but does not necessarily cause complete clogging. The determined intrinsic biomass permeability of **100 ± 50 mD** indicates that biomass can remain hydraulically conductive and may therefore sustain advective nutrient supply through or around microbial structures [5].

Under unsaturated conditions, the controlling limitation shifts from bulk hydraulic conductivity toward interfacial transport. Although the gas phase provides rapid advective delivery of H_2 and CO_2, microbial conversion requires dissolution into the aqueous phase and access to active biomass. The reactor model and dimensionless analysis therefore indicate that methane production is governed mainly by gas–liquid transfer, brine connectivity, and the spatial overlap between gas, liquid, and biomass [6]. This supports the interpretation of the micromodel as a reactive lab-on-a-chip reactor, where the efficiency is controlled by the quality of phase contact rather than by gas supply alone.

The dimensionless analysis provides a useful framework to generalize these observations. Péclet and Damköhler numbers separate regions dominated by advection, diffusion, or reaction, while Sherwood and Thiele-type metrics help distinguish external mass-transfer limitations from internal biomass diffusion effects. For the investigated operating window, the results suggest that external transfer and interfacial renewal are more critical than internal diffusion through the biomass. This finding is particularly relevant for scale-up, because improving conversion efficiency may require controlling saturation patterns and gas–brine contact area rather than simply increasing injection rate.

A key implication is that biomass accumulation has a dual role. It may reduce effective pore volume and locally redirect flow, but it also creates reactive zones and can remain permeable enough to sustain substrate delivery. Therefore, geomethanation should not be viewed only as a bio-clogging risk or only as a microbial conversion process. It is better described as a coupled bio-reactive transport problem in which moderate biomass accumulation may support conversion, while excessive or poorly distributed growth may impair injectivity and reduce reactor efficiency.

Future work should focus on extending the workflow toward more reservoir-representative conditions. This includes testing higher pressures, broader salinity ranges, realistic rock-derived pore geometries, and cyclic injection–production schemes. Particular attention should be given to saturation control, because brine distribution determines both microbial habitat and gas–liquid interfacial area.

The reactor model should also be expanded from a lumped description toward spatially resolved reactive transport, where local biomass density, interfacial area, and substrate gradients are coupled directly to methane formation. This would allow dimensionless maps to be used not only for interpretation, but also for predicting operating windows for efficient geomethanation.

Finally, the workflow should be translated from micromodels to core-scale and reservoir-scale models. The intrinsic biomass permeability and transport-regime descriptors obtained here provide parameters that can support upscaling. In this way, pore-scale experiments can help define how depleted gas reservoirs may be operated as controllable subsurface bioreactors for converting H_2 and CO_2 into CH_4.

References

1. E. Thaysen, S. McMahon, G. Strobel, I. Butler, B. Ngwenya, N. Heinemann, M. Wilkinson, A. Hassanpouryouzband, C. McDermott, K. Edlmann, Renew. Sustain. Energy Rev. 151 (2021).
2. G. Strobel, B. Hagemann, T.M. Huppertz, L. Ganzer, Renew. Sustain. Energy Rev. 123, 109747 (2020).
3. D. Zivar et al., Int. J. Hydrogen Energy 46, 23436–23462 (2021).
4. A. Zauner, K. Fazeni-Fraisl, P. Wolf-Zoellner, A. Veseli, M.-T. Holzleitner, M. Lehner, S. Bauer, M. Pichler, Energies 15 (2022).
5. P. Jasek, H. Konegger, A.P. Loibner, H. Ott, Int. J. Hydrogen Energy 157, 150191 (2025).
6. P. Jasek, G. Stiedl, H. Ott, *Transport and Microbial Controls on Subsurface Hydrogen Methanation Revealed by Microfluidic Experiments and Simulation* (preprint submitted to *Int. J. Hydrogen Energy*).
7. S. Bottero, T. Storck, T.J. Heimovaara, M.C.M. van Loosdrecht, M.V. Enzien, C. Picioreanu, Biofouling 29, 1069–1086 (2013).
8. J. Hommel, E. Coltman, H. Class, Transport Porous Media 124, 589–629 (2018).

9. C.-Z. Qin, S.M. Hassanizadeh, Transport Porous Media 110, 345–367 (2015).
10. M. Thullner, P. Baveye, Biotechnol. Bioeng. 99, 1337–1351 (2008).
11. T.R. Pintelon, C. Picioreanu, M.C. van Loosdrecht, M.L. Johns, Biotechnol. Bioeng. 109, 1031–1042 (2012).
12. H.-C. Flemming, J. Wingender, U. Szewzyk, P. Steinberg, S.A. Rice, S. Kjelleberg, Nat. Rev. Microbiol. 14, 563–575 (2016).
13. N. Hassannayebi, B. Jammernegg, J. Schritter, P. Arnold, F. Enzmann, M. Kersten, A.P. Loibner, M. Fernø, H. Ott, Transport Porous Media 139, 579–593 (2021).
14. A. Valiei, A. Kumar, P. Mukherjee, Y. Liu, T. Thundat, Lab Chip 12, 5133–5137 (2012).
15. W. Deng, M.B. Cardenas, M.F. Kirk, S.J. Altman, P.C. Bennett, Environ. Sci. Technol. 47, 11092–11098 (2013).
16. D.L. Kurz, E. Secchi, F.J. Carrillo, I.C. Bourg, R. Stocker, J. Jimenez-Martinez, Proc. Natl. Acad. Sci. U.S.A. 119, e2122202119 (2022).
17. R. Sander, Atmos. Chem. Phys. 23, 10901–12440 (2023).
18. A. Akgerman, J.L. Gainer, J. Chem. Eng. Data 17, 372–377 (1972).
19. S. Langenberg, T. Carstens, D. Hupperich, S. Schweighoefer, U. Schurath, Atmos. Chem. Phys. 20, 3669–3682 (2020).
20. J.M.P.Q. Delgado, Chem. Eng. Res. Des. 85, 1245–1252 (2007).
21. E.W. Thiele, Ind. Eng. Chem. 31, 916–920 (1939).
22. B. Godongwana, PLoS ONE 11, e0153000 (2016).
23. A. Moser, *Bioprocess Technology: Kinetics and Reactors*, Springer Science & Business Media (2012).
24. M.B. Jensen, L.D.M. Ottosen, M.V.W. Kofoed, Renew. Sustain. Energy Rev. 147, 111209 (2021).
25. R. Zaveri, R. Easter, J. Shilling, J. Seinfeld, Atmos. Chem. Phys. 14, 5153–5181 (2014).
26. J. Zhu, S.S. Araya, X. Cui, S.K. Kær, Int. J. Hydrogen Energy 47, 8700–8715 (2022).